# Giant tunable Rashba spin splitting in a two-dimensional BiSb monolayer and in BiSb/AlN heterostructures

Sobhit Singh* and Aldo H. Romero†

*Department of Physics and Astronomy, West Virginia University, Morgantown, West Virginia 26505-6315, USA*

(Received 31 January 2017; published 25 April 2017)

The search for novel two-dimensional giant Rashba semiconductors is a crucial step in the development of the forthcoming nanospintronic technology. Using first-principles calculations, we study a stable two-dimensional crystal phase of BiSb having buckled honeycomb lattice geometry, which is yet unexplored. The phonon, room temperature molecular dynamics, and elastic constant calculations verify the dynamical and mechanical stability of the monolayer at 0 K and at room temperature. The calculated electronic band structure reveals the direct band gap semiconducting nature of a BiSb monolayer with the presence of a highly mobile two-dimensional electron gas (2DEG) near the Fermi level. Inclusion of spin-orbit coupling yields the giant Rashba spin-splitting of a 2DEG near the Fermi level. The calculated Rashba energy and Rashba splitting constant are 13 meV and 2.3 eVÅ, respectively, which are amongst the largest yet known Rashba spin splitting parameters in 2D materials. We demonstrate that the strength of the Rashba spin splitting can be significantly tuned by applying in-plane biaxial strain on the BiSb monolayer. The presence of the giant Rashba spin splitting together with the large electronic band gap (1.6 eV) makes this system of peculiar interest for optoelectronics applications. Furthermore, we study the electronic properties of BiSb/AlN heterostructures having a lattice mismatch of 1.3% at the interface. Our results suggest that a BiSb monolayer and BiSb/AlN heterostructure systems could be potentially used to develop highly efficient spin field-effect transistors, optoelectronics, and nanospintronic devices. Thus, this comprehensive study of two-dimensional BiSb systems can expand the range of possible applications in future spintronic technology.

DOI: 10.1103/PhysRevB.95.165444

## I. INTRODUCTION

Discovery of new materials having large spin-orbit coupling (SOC) is very crucial in the rapidly burgeoning field of spintronics. In spintronics, we exploit the spin-orbit interaction present in materials to tune their electronic properties. The spin-orbit interaction originates due to the relativistic motion of electrons and acts as an effective built-in magnetic field in nonmagnetic materials, which functions similar to the external magnetic field in the celebrated quantum Hall effect [1,2]. Electrons with opposite spins feel an opposite magnetic field in their rest frame and this field couples to their magnetic moment. Nevertheless, the net effects do not cancel out but yield a new quantum phenomenon called the Rashba effect [3]. The Rashba effect appears in systems with broken inversion-symmetry and causes lift in the spin degeneracy of electronic bands. Initially, the Rashba effect was believed to arise at the surfaces and interfaces due to the asymmetry of the confinement potential. However, recent works reveal that the Rashba effect can also be realized in bulk semiconductors [4–10] and hybrid organic-inorganic perovskites [11–13].

The strength of the Rashba effect can be quantized by three key parameters: the Rashba energy ($E_R$), the Rashba momentum ($k_o$), and the Rashba constant ($\alpha_R$). Materials with a large Rashba energy and a large Rashba constant provide us more opportunities to tune their spintronic properties. Experiments report the presence of two-dimensional (2D) Rashba spin-splitting in InAlAs/InGaAs [14] and $LaAlO_3/SrTiO_3$ [15,16] interfaces. However, the magnitude of the Rashba constant ($\alpha_R$) is not large in the mentioned interfaces ($\alpha_R = 0.07$ eVÅ for InAlAs/InGaAs [14] and $\alpha_R = 0.01$–$0.05$ eVÅ for the $LaAlO_3/SrTiO_3$ oxide interface [15,16]). Currently, surfaces of heavy metals such as Au, Bi, Ir, and BiAg(111) alloys are known to exhibit large Rashba spin splitting. The magnitude of $\alpha_R$ in Au(111) [17], Bi(111) [18], Ir(111) [19], and BiAg(111) [20] surfaces is 0.33, 0.55, 1.3, and 3.05 eVÅ, respectively. Even though these surfaces inherit large Rashba spin splitting, yet they cannot be used in many spintronics device applications due to the presence of the (semi)metallic surface states. In particular, there is still no stable 2D semiconductor having a large Rashba effect which is suitable for spin field-effect transistor applications.

In addition to the spintronic applications, the 2D semiconductors inheriting large Rashba effects are strongly desired to hunt Majorana fermions. A 2D Rashba semiconductor interfaced with an $s$-wave superconductor under broken time-reversal symmetry can be used to build topological heterostructures that can support the long-sought but not yet detected Majorana fermions [21–23]. Majorana fermions manifest themselves as a zero-bias conductance peak [24]. If experimentally realized, Majorana fermions may pave the way for the realization of fault-tolerant topological quantum computation [25–27]. Therefore, there is a huge demand to search for new stable materials inheriting large controllable Rashba effects in two dimensions.

In the present work, we study the electronic properties of a BiSb monolayer by means of first-principles calculations. Our calculations reveal that a BiSb monolayer forms a stable free-standing 2D crystal and exhibits a giant controllable Rashba effect. The observed $E_R$ and $\alpha_R$ are 13 meV and 2.3 eVÅ, respectively, which are amongst the largest yet known Rashba spin splitting parameters in 2D materials

*smsingh@mix.wvu.edu
†alromero@mail.wvu.edu

 

[14–20,28–35]. We demonstrate that the Rashba effect in a BiSb monolayer can be efficiently tuned by applying biaxial strain. The calculated energy band gap is 1.6 eV, which lies in the visible range. The presence of the giant Rashba spin splitting together with a large electronic band gap makes this system of peculiar interest for optoelectronics applications. We further investigate the electronic properties of a BiSb monolayer placed in contact with an AlN substrate. We construct BiSb/AlN heterostructures with two possible layer terminations (Bi and Sb) at the interface. Both BiSb/AlN van der Waals (vdW) heterostructures are found to exhibit a direct band gap semiconducting nature with the presence of a light mobile two-dimensional electron gas (2DEG) at the interface. Remarkably, we notice signatures of the giant Rashba spin splitting of a 2DEG near the Fermi level. Our results suggest that a BiSb monolayer and BiSb/AlN heterostructure systems could be potentially used to develop highly efficient spin field-effect transistors, optoelectronics, and nanospintronic devices.

## II. COMPUTATIONAL DETAILS

Density functional theory (DFT) [36,37] based first-principles calculations were carried out using the projector augmented-wave (PAW) method as implemented in the VASP code [38,39]. We used the PBE exchange-correlation functional as parametrized by Perdew-Burke-Ernzerhof [40]. The SOC was employed by a second-variation method implemented in the VASP code. We considered 15 valence electrons of Bi ($5d^{10}6s^26p^3$) and 5 valence electrons of Sb ($5s^25p^3$) in the PAW pseudopotential. The lattice parameters of the monolayer were optimized until the Hellmann-Feynman residual forces were less than $10^{-4}$ eV/Å per atom. For convergence of the electronic self-consistent calculations, a total energy difference criterion was defined as $10^{-8}$ eV. We used 650 eV as the kinetic energy cutoff of the plane wave basis set and a Γ-type $10 \times 10 \times 1$ $k$-point mesh was employed to optimize the lattice parameters and the self-energy. The phonon calculations were performed for a $4 \times 4 \times 1$ supercell using the density functional perturbation theory (DFPT) approach as implemented in the VASP code. The PHONOPY code [41] was used for phonons postprocessing. SOC was included in phonon calculations as well as in the optimization of the primitive cell. To verify the stability of the BiSb monolayer at room temperature, we performed room temperature molecular dynamics (MD) simulations for more than 6000 fs with a time step of 1 fs. In MD simulations, we employed a supercell of size $4 \times 4 \times 1$ to guarantee the decay of interatomic force constants within the supercell dimensions. To investigate the effect of in-plane biaxial strain, we varied the $a$ and $b$ lattice vectors from −8% (compression) to +8% (expansion) while performing relaxation of the inner coordinates. The screened hybrid Heyd-Scuseria-Ernzerhof (HSE06) functional [42,43] was used to get a better estimation of the electronic band gap of the BiSb monolayer. The Bi- and Sb-terminated BiSb/AlN heterostructures were modeled by using supercells of size $(3 \times 3 \times 1)/(4 \times 4 \times 1)$. This combination yields a lattice mismatch of 1.3%. The vdW interaction [44,45] together with SOC as implemented in the VASP code was included in the structural optimization as well as in the electronic structure calculations reported for BiSb/AlN heterostructures. The heterostructures were optimized until the total residual forces on each atom were less than 0.001 eV/Å. A Γ $k$-point mesh of size $8 \times 8 \times 1$ was used to sample the irreducible Brillouin zone of the heterostructures. A vacuum of thickness larger than 15 Å was added along the $c$ axis to avoid any interaction between two periodic BiSb and BiSb/AlN geometries. The PYPROCAR code was used to calculate the constant energy contour plots of the spin texture [46].

## III. RESULTS AND DISCUSSION

### A. Crystal structure and the stability of the BiSb monolayer

The bulk BiSb compound is known to exhibit a rhombohedral structure with $R3m$ symmetry in its ground state [47,48]. In this geometry, Bi and Sb atoms are stacked along the (111) direction of a rhombohedral primitive cell. Two alternative Bi and Sb layers strongly interact covalently and form a BiSb bilayer, whereas two adjacent BiSb bilayers weakly interact due to the weak vdW interaction. Therefore, it is possible to fabricate a stable two-dimensional BiSb monolayer by advanced exfoliation, vapor deposition, or molecular-beam epitaxy techniques. A detailed study of the structural, vibrational, electronic, thermoelectric, and topological behavior of bulk BiSb can be found in Refs. [47,48]. Bulk BiSb exhibits a giant Rashba effect with the presence of the pressure-driven Weyl semimetallic phase [48]. This is one of the first predicted ferroelectric Weyl semimetals which demonstrates tunability of Weyl charges. Such unique and intriguing topological features of bulk BiSb stimulate research in the two-dimensional BiSb.

Figures 1(a)–1(c) show the crystal structure of an isolated BiSb monolayer. The fully optimized structure exhibits a buckled honeycomb lattice having a threefold rotational symmetry in the $P3m1$ space group (156). The optimized lattice parameters are $a = b = 4.255$ Å. The Bi-Sb bond length ($d$) and the buckling height ($h$) are 2.98 and 1.69 Å, respectively. The Bi-Sb-Bi bond angle is 91.2°. In order to test the energetic stability of BiSb monolayers, we calculate the formation energy of a single optimized BiSb monolayer using the following expression:

$$E_{\text{formation}} = \frac{E_{\text{coh}}(BiSb) - xE_{\text{coh}}(Bi) - yE_{\text{coh}}(Sb)}{(x+y)}, \quad (1)$$

where $E_{\text{coh}}$ denotes the cohesive energy relative to the free constituent atom, and $x$ and $y$ represent the total number of Bi and Sb atoms in the cell, respectively. The calculated formation energy ($E_{\text{formation}}$) of a single BiSb monolayer is −2.23 eV/atom, which is lower than the formation energy of most of the previously synthesized single layer transition-metal dichalcogenides [49]. For example, the formation energy of single layer $MoS_2$, $MoSe_2$, $MoTe_2$, $WS_2$, $WSe_2$, $WTe_2$, $NbTe_2$, and $NbSe_2$ is −0.83, −0.75, −0.30, −0.91, −0.62, −0.10, −0.42, and −0.88 eV/atom, respectively [50]. However, the formation energy of the BiSb monolayer is slightly larger than that of other binary V-V monolayer compounds such as PN, AsN, SbN, AsP, SbP, and SbAs [51]. Nonetheless, the BiSb monolayer forms an energetically stable crystal structure and therefore it can be synthesized in laboratory.

We test the dynamical stability of the BiSb monolayer by analyzing the phonon spectra. Figure 1(d) represents the

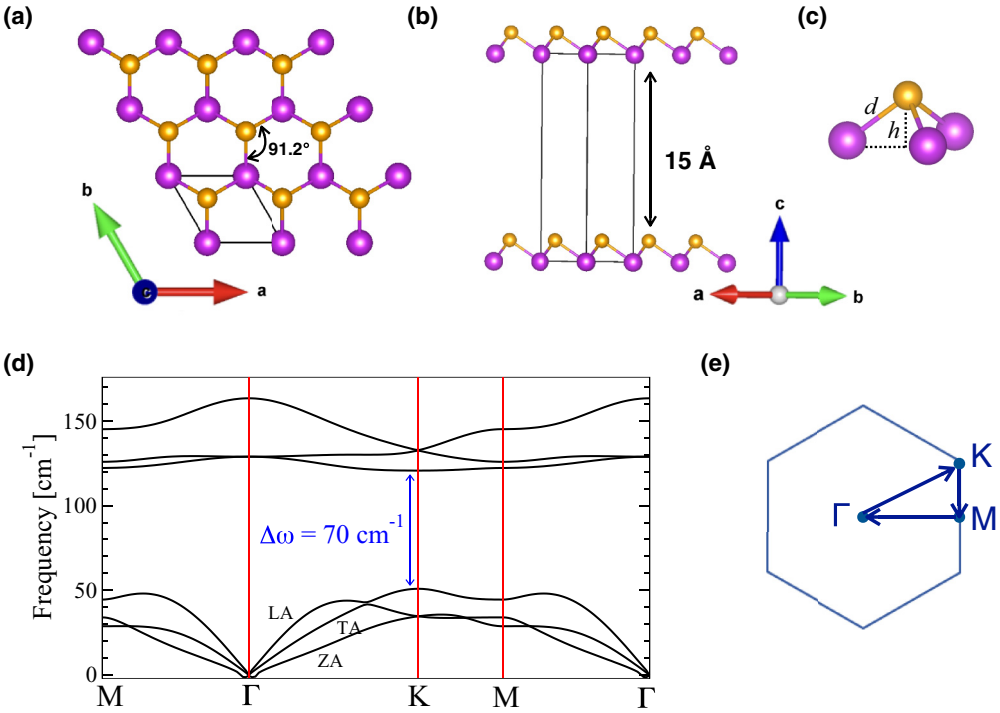


FIG. 1. Panels (a) and (b) represent the honeycomb crystal structure of the BiSb monolayer viewed from the top and side directions. Bi atoms are shown in purple while Sb atoms are shown in orange. (c) Bonding of Bi-Sb atoms. Here, $d$ represents the Bi-Sb bond length and $h$ represents the buckling height. (d) The phonon spectra of the BiSb monolayer calculated along the high-symmetry directions of the Brillouin zone. (e) The hexagonal 2D Brillouin zone labeled with high-symmetry points.

phonon band structure calculated along the high-symmetry directions of the Brillouin zone shown in Fig. 1(e). We notice that there are three optical and three acoustical phonon branches, corresponding to a total of six branches due to two atoms per cell. The longitudinal acoustic (LA) and transverse acoustic (TA) modes represent in-plane vibrations while the ZA branch corresponds to the out-of-plane vibrations. One can notice that all phonon frequencies are positive, which confirms the dynamical stability of the BiSb monolayer at 0 K. It is worth noting that the ZA phonon branch exhibits a small imaginary frequency having a 'U'-shape near the Γ point. This U-shape feature does not correspond to the lattice instability, nevertheless it is a signature of the flexural acoustic mode present in two-dimensional systems [52]. The flexural acoustic modes are known to play a crucial role in governing the thermal and mechanical properties of 2D systems. Such a U-shape feature near the Γ point has been observed in many other similar 2D systems studied earlier [51,53,54]. Thus, our phonon calculations confirm that the BiSb monolayer is dynamically stable and, therefore, it can exist as a free-standing 2D crystal. Furthermore, we notice that the acoustic and optical phonon branches are well separated, indicating a good optical response of the BiSb monolayer. There is a wide direct frequency gap ($\Delta\omega$) of 70 cm$^{-1}$ between the optical and acoustic phonon modes at the K point. In the photoexcitation experiments and in the solar cell applications, the excitons (photon excited electron-hole pairs) loose most of their energy by exciting the optical phonons. These excited optical phonons further decay into the acoustic phonons which carry the heat away. Notably, in our case the phonon frequency gap is larger than the frequency of the hardest acoustic phonon mode (~50 cm$^{-1}$). This feature significantly avoids the Klemens decay [55], which indicates the possibility to use such types of materials for the high-efficiency solar cell applications [56].

From the application point of view, it is important to check the mechanical stability of any new material. Therefore, we have performed first-principles calculations to determine the elastic constants ($C_{ij}$) of the BiSb monolayer. The elastic constants were calculated using the stress-strain relations as implemented in the VASP code [38,39]. We used a dense 21 × 21 × 1 Γ-$k$-mesh to reduce the numerical errors caused by in-plane strain of the system. The second Piola-Kirchhoff stress method was used to determine the elastic constants in 2D with units of N/m [57,58]. We find that $C_{11} = 24.4$ N/m and $C_{12} = 5.8$ N/m. We further calculated the 2D layer modulus ($\gamma$), Young's modulus ($Y_S^{2D}$), and Poisson's ratio ($\nu$) using the method suggested by Andrew *et al.* [59]. The obtained values of $\gamma$, $Y_S^{2D}$, and $\nu$ are 15.12 N/m, 23.0 N/m, and 0.24, respectively. Poisson's ratio is larger compared to that of h-BN (0.22) and graphene (0.17) monolayers; however, $\nu$ is smaller compared to that of buckled Si (0.34) and Ge (0.28) monolayers [59]. The $\gamma$ and $Y_S^{2D}$ values of the BiSb monolayer are significantly lower than those of h-BN and graphene. This is due to the fact that Bi-Sb bonds are weaker compared to B-N and C-C bonds. However, all the obtained elastic constants are positive, confirming the mechanical stability of the BiSb monolayer. A detailed study of the mechanical properties of a strained BiSb monolayer will be published elsewhere.

We further perform the *ab initio* MD simulations to assess the thermal stability of the BiSb monolayer at room temperature. Figure 2 shows the mean-square displacement of the Bi and Sb atoms as a function of the simulation time

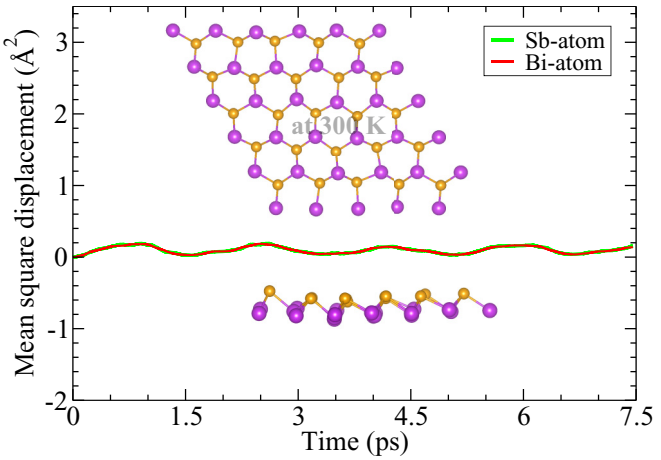


FIG. 2. This figure shows variation in the mean-square displacement of Bi (purple) and Sb (orange) atoms as a function of simulation time at 300 K. Insets show the top and side views of the geometric structures of the monolayer at the end of the MD simulation at 300 K.

(in ps). The snapshots of the geometric structure at 300 K obtained at the end of the MD simulation (total time = 7.5 ps) are also given in the insets of Fig. 2. We see that the mean-square displacement oscillates with an amplitude of about 2% of the total Bi-Sb bond length. Additionally, one can notice that the geometric structures at 0 K (Fig. 1) and at 300 K (insets of Fig. 2) are quite similar. This confirms the thermodynamical stability of the BiSb monolayer at room temperature, suggesting the possible applicability of this system for room temperature device applications.

It is worth mentioning that, although the energetic stability tests indicate that the proposed BiSb monolayer structure is quite robust against small lattice defects, vacancies, impurities, and structural deformations, the situation might change in different ambient environments. Most of the recently discovered 2D systems exhibit significant structural deformations under different ambient conditions. A more detailed investigation is required to understand the effect of the ambient environment on the structural stability and electronic properties of BiSb monolayers.

### B. Electronic structure: The giant 2D Rashba spin splitting

Figure 3 shows the electronic band structure of the BiSb monolayer calculated using (a) Generalized Gradient Approximation (GGA) and (b) GGA + SOC approximations. Without SOC, the band structure reveals the semiconducting nature with the presence of a direct band gap ($E_g$) of 0.95 eV at the Γ point. However, bulk BiSb is known to exhibit an indirect band gap semiconducting nature [48]. The thickness-dependent transition from an indirect (3D) to a direct (2D) band gap semiconductor is not new in layerlike systems, and it has already been reported for other layerlike systems [60]. In the BiSb monolayer, the conduction band bottom (CBB) shows a parabolic nature near the Γ point

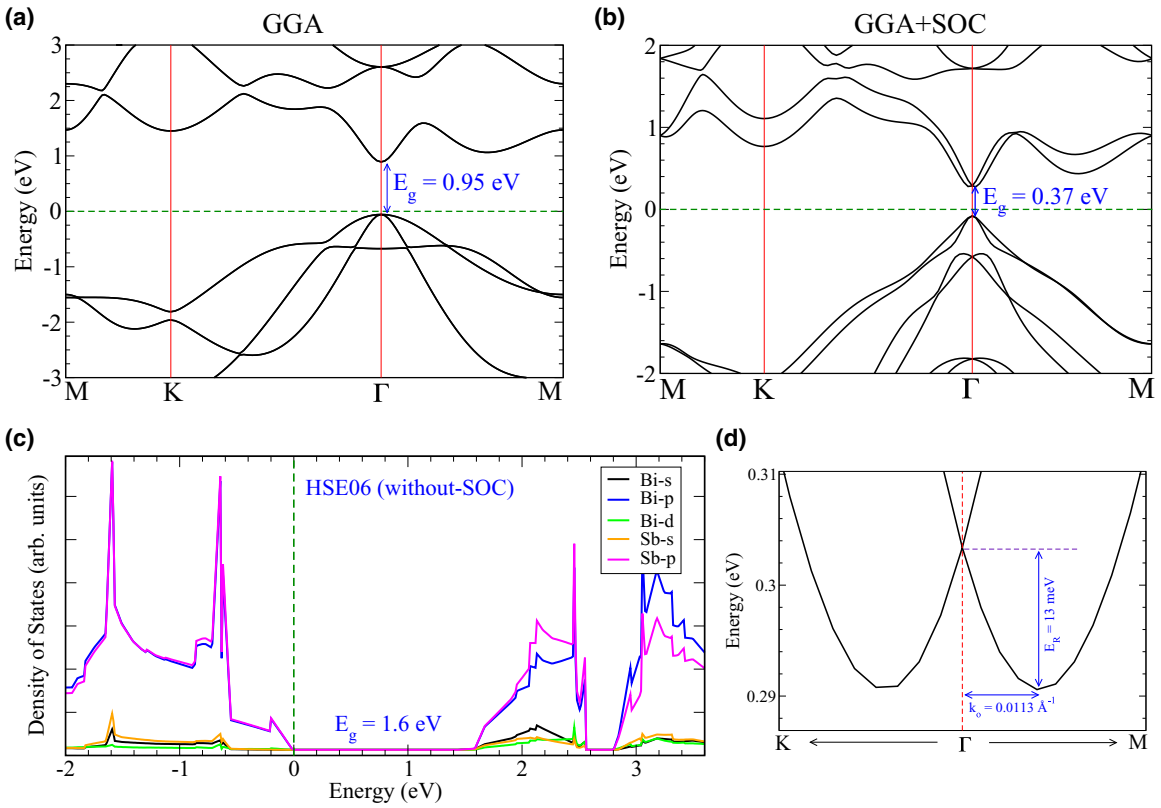


FIG. 3. The electronic band structure of a BiSb monolayer: (a) without SOC and (b) with SOC. (c) The atomic orbital projected DOS calculated using the HSE06 approximation and a Γ $k$-mesh of size 21 × 21 × 1. (d) The enlarged view of Rashba spin splitting of conduction bands near the Fermi level. The green dotted line represents the Fermi level.

indicating the presence of highly mobile light electrons (nearly free electrons), while the valence band top (VBT) indicates the presence of relatively heavy holes near the Γ point. Since DFT is known to underestimate the energy band gap, we employ the Heyd-Scuseria-Ernzerhof (HSE06) hybrid functional to predict a more reasonable energy band gap. Figure 3(c) shows the orbital projected density of states (DOS) calculated using the HSE06 approximation (without SOC) for the BiSb monolayer. We find that the HSE06 band gap is approximately 1.6 eV, which is larger than the DFT (GGA and GGA + SOC) predicted band gap and lies in the visible range of the electromagnetic spectrum. This makes this system of peculiar interest for optoelectronic applications. It is worth mentioning that the HSE06 functional only enhances the band gap without any notable change in the shape of the electronic bands and the strength of the Rashba spin splitting [6]. Our calculations further indicate that the bands near the Fermi level ($E_F$) are mainly composed of Bi $6p$ and Sb $5p$ orbitals.

Inclusion of SOC results in the spin splitting of the electronic bands [Fig. 3(b)]. Remarkably, we notice a Rashba-type spin splitting of the CBB near the Γ point, while the VBT remains degenerate [Figs. 3(b) and 3(d)]. Also, the direct DFT band gap at the Γ point decreases to 0.37 eV. To quantitatively determine the strength of the Rashba spin splitting, we calculate the Rashba parameters as described in Ref. [6]. We find that $E_R = 13$ meV, $k_o = 0.0113$ Å$^{-1}$, and $\alpha_R = 2E_R/k_o = 2.3$ eVÅ. This is amongst the largest Rashba spin splitting in 2D materials reported so far. For example, the reported Rashba energy (Rashba constant) for the Au(111) surface, the InGaAs/InAlAs interface, the $LaAlO_3/SrTiO_3$ oxide interface, and the Bi(111) surface is 2.1 meV (0.33 eVÅ) [17], 0.98 meV (0.07 eVÅ) [14], <5 meV (0.01–0.05 eVÅ) [15,16], and 14 meV (0.55 eVÅ) [18], respectively. One can notice that the Bi(111) surface exhibits the largest Rashba spin splitting ($E_R = 14$ meV) amongst all the above-listed systems. However, the semimetallic nature of the Bi(111) surface limits its applications in the spintronic devices [18,61]. The BiSb monolayer overcomes this limitation due to its direct band gap semiconducting nature coupled with the large Rashba spin splitting, which is comparable with the Rashba spin splitting of the Bi(111) surface. Interestingly, we notice that the Rashba spin splitting of the BiSb monolayer is even comparable with some of the known bulk Rashba semiconductors such as $BiAlO_3$($E_R = 7.34$–$8.62$ meV, $\alpha_R = 0.39$–$0.74$ eVÅ [10]), BiTeI ($E_R = 100$ meV, $\alpha_R = 3.8$ eVÅ [4]), BiTeCl ($E_R = 18.5$ meV, $\alpha_R = 1.2$ eVÅ [8]), GeTe ($E_R = 227$ meV, $\alpha_R = 4.8$ eVÅ [6]), SnTe ($E_R = 272$ meV, $\alpha_R = 6.8$ eVÅ [7]), LiZnSb ($E_R = 21$ meV, $\alpha_R = 1.82$ eVÅ [9]), and KMgSb ($E_R = 10$ meV, $\alpha_R = 0.83$ eVÅ [9]).

The origin of the large Rashba effect in the present BiSb structure can be understood by looking at the symmetry of the orbitals near the Fermi level. The orbital projected DOS plot shown in Fig. 3(c) reveals that the states near Fermi level have same orbital symmetry. Therefore, these states could strongly

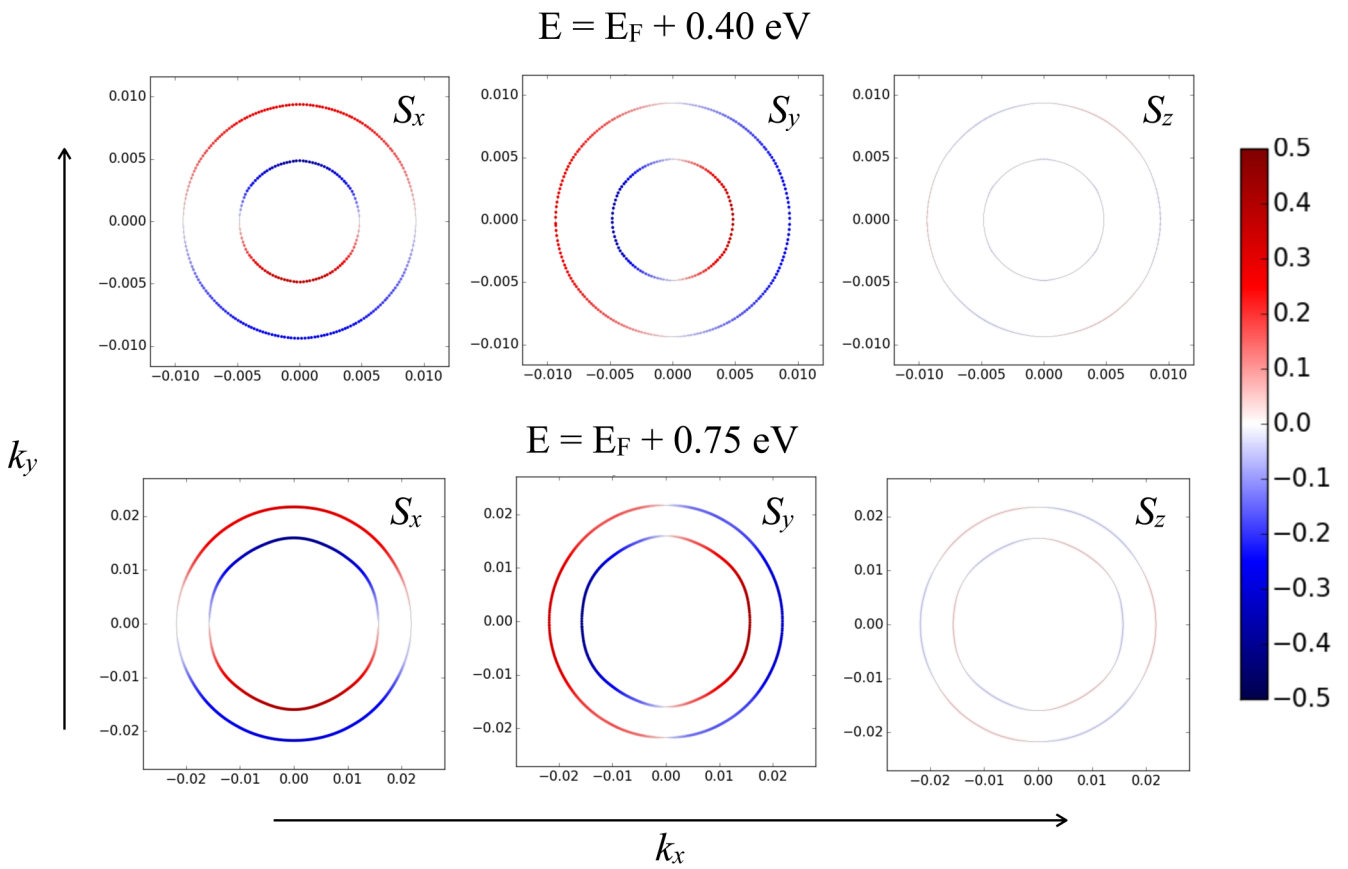


FIG. 4. Spin projected constant energy contour plots of spin texture calculated in a $k_x$-$k_y$ plane centered at the Γ point. Top (bottom) row represents the spin textures calculated at an energy surface 0.40 eV (0.75 eV) above the Fermi level. In the color scale, red depicts spin-up states while blue depicts spin-down states.

couple and yield large Rashba spin splitting, as predicted by the $\mathbf{k}\cdot\mathbf{p}$ theory in Ref. [5]. Thus, after comparing the strength of the Rashba spin splitting in the BiSb monolayer and several other known large Rashba semiconductors, one can realize that the Rashba spin splitting of the highly mobile light electrons in the BiSb monolayer is indeed remarkable and, therefore, this system can be used to make efficient advanced spin field-effect transistors.

Figure 4 shows the constant energy 2D contour plots of spin texture calculated in a $k_x$-$k_y$ plane centered at the Γ point. Evidently, one can notice the Rashba-type spin splitting of spin-up (red) and spin-down (blue) electronic bands. The concentric spin-texture circles are the result of the purely 2D Rashba spin splitting present above the Fermi level (conduction bands). A further analysis of the projection of different spin components ($S_x$, $S_y$, and $S_z$) on the electronic bands reveals that only in-plane $S_x$ and $S_y$ spin components are present in the Rashba spin split bands, without the presence of any out-of-plane $S_z$ component. This further confirms that the spin splitting of electrons in the BiSb monolayer has a purely 2D Rashba nature. Interestingly, we observe the Rashba spin splitting at significantly large energies (0.40 and 0.75 eV) above the Fermi level.

### C. Effect of in-plane biaxial strain on the electronic properties

It is very important to study the effect of the biaxial strain on the electronic properties before we shift our concentration to the BiSb/AlN heterostructure systems. Therefore, we study the strained BiSb monolayers by applying biaxial strain ($x$) ranging from $-8\%$ (compression) to $+8\%$ (elongation) on the $a$ and $b$ lattice vectors. Figure 5 shows changes in the with- and without-SOC electronic band structures with respect to $x = +2\%$ (solid blue lines), $-2\%$ (broken magenta line), and $-6\%$ (solid orange lines) biaxial strains. From Figs. 5(a) and 5(b), we notice that the system retains its direct band gap semiconducting nature until $x = -2\%$. However, with further increase in biaxial strain, it changes to an indirect band gap semiconductor at $-4\%$ and, eventually, we realize a metallic phase-transition at $x = -6\%$. Furthermore, the degeneracy of the valence band near the Γ point breaks down at $x = -6\%$ biaxial compression and a Rashba-type spin splitting appears in the valence band states. Analysis of the Rashba spin splitting in the strained bands evinces that the Rashba energy (constant) decreases from 13 meV (2.3 eVÅ) to 9.21 meV (1.77 eVÅ) with an increase in the biaxial compression from $x = 0\%$ to $x = -4\%$. However, we observe a significant increase in the Rashba spin-splitting parameters with increasing biaxial elongation (for $x = +6\%$ elongation: $E_R = 33.4$ meV, $\alpha_R = 3.56$ eVÅ). Consequently, one can significantly tune the strength of the Rashba spin splitting by varying the in-plane biaxial strain. Nonetheless, in order to experimentally realize the novel direct band gap Rashba semiconducting properties of the BiSb monolayer, we must grow this system on top of a substrate such that the lattice mismatch is less than 2%. This can be experimentally realized by a proper choice of substrate material.

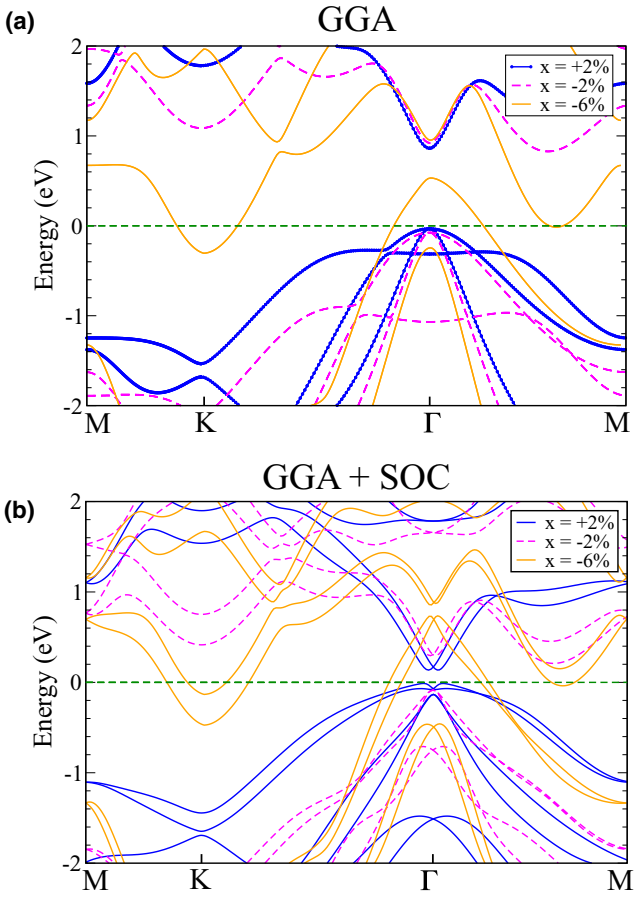


FIG. 5. The electronic band structure of strained BiSb monolayers at an applied in-plane biaxial strain $x = +2\%$ (stretched) and $-2\%$ and $-6\%$ (compressed) monolayers, (a) without SOC and (b) with SOC. The horizontal, green dotted line represents the Fermi level.

### D. BiSb/AlN heterostructures

How do the electronic properties of a BiSb monolayer change in the presence of another substrate material? Can we still realize the Rashba spin-splitting of 2DEG present at the interface of heterostructure systems? How would the energetic stability of an isolated BiSb monolayer change in the presence of another contact material? In order to address these questions, we model BiSb/AlN heterostructures and study their electronic properties. To minimize the lattice mismatch between two stackings, we build the heterostructure using a $4 \times 4 \times 1$ supercell of AlN and a $3 \times 3 \times 1$ supercell of BiSb. Thus the obtained lattice mismatch is 1.3%. One could also use hexagonal BN or GaN as a substrate material for a BiSb monolayer. The lattice mismatches for BiSb($3 \times 3 \times 1$)/BN($5 \times 5 \times 1$) and BiSb($3 \times 3 \times 1$)/GaN($4 \times 4 \times 1$) combinations are 1.7% and 2.15%, respectively. In the present work, we study the BiSb/AlN heterostructure system because this system exhibits minimum lattice mismatch. Figure 6 shows the BiSb/AlN heterostructures with two possible layer terminations at the interface: first, Bi termination [Fig. 6(a)], and second, Sb termination [Fig. 6(b)]. The vdW optimized lattice constants for Bi- and Sb-terminated interfaces are 12.541 and 12.536 Å, respectively. In both cases, the BiSb lattice is being compressed

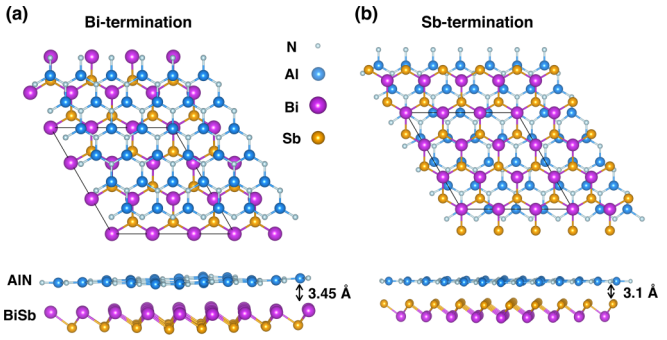


FIG. 6. This figure represents the relaxed geometric structures of BiSb/AlN heterostructures with two possible terminations at the interface. Panel (a) shows the top and side views of a Bi-terminated interface while panel (b) shows the top and side views of an Sb-terminated interface.

by 1.8% while the AlN lattice is being stretched by 0.5%. The interlayer spacing between AlN and BiSb monolayers is 3.45 Å (3.10 Å) for Bi-terminated (Sb-terminated) interfaces. The presence of larger interlayer spacing for the Bi-terminated interface can be ascribed to the fact that the Bi atom has a larger covalent radius compared to that of the Sb atom.

The calculated formation energies for Bi- and Sb-terminated interfaces are −2.59 and −2.60 eV/atom, respectively. This suggests that the Sb-terminated interface is energetically 10 meV/atom more favorable compared to the Bi-terminated interface. Furthermore, comparing the formation energy of an isolated BiSb monolayer with that of a BiSb/AlN system, we notice that the BiSb/AlN heterostructures are energetically more stable than a single sheet of BiSb. One can switch the ferroelectric polarization, and thus the electric field direction at the interface, by switching the Bi and Sb layers. An inverted ferroelectric polarization leads to the complete inversion of the spin-polarized Rashba bands near the Fermi level.

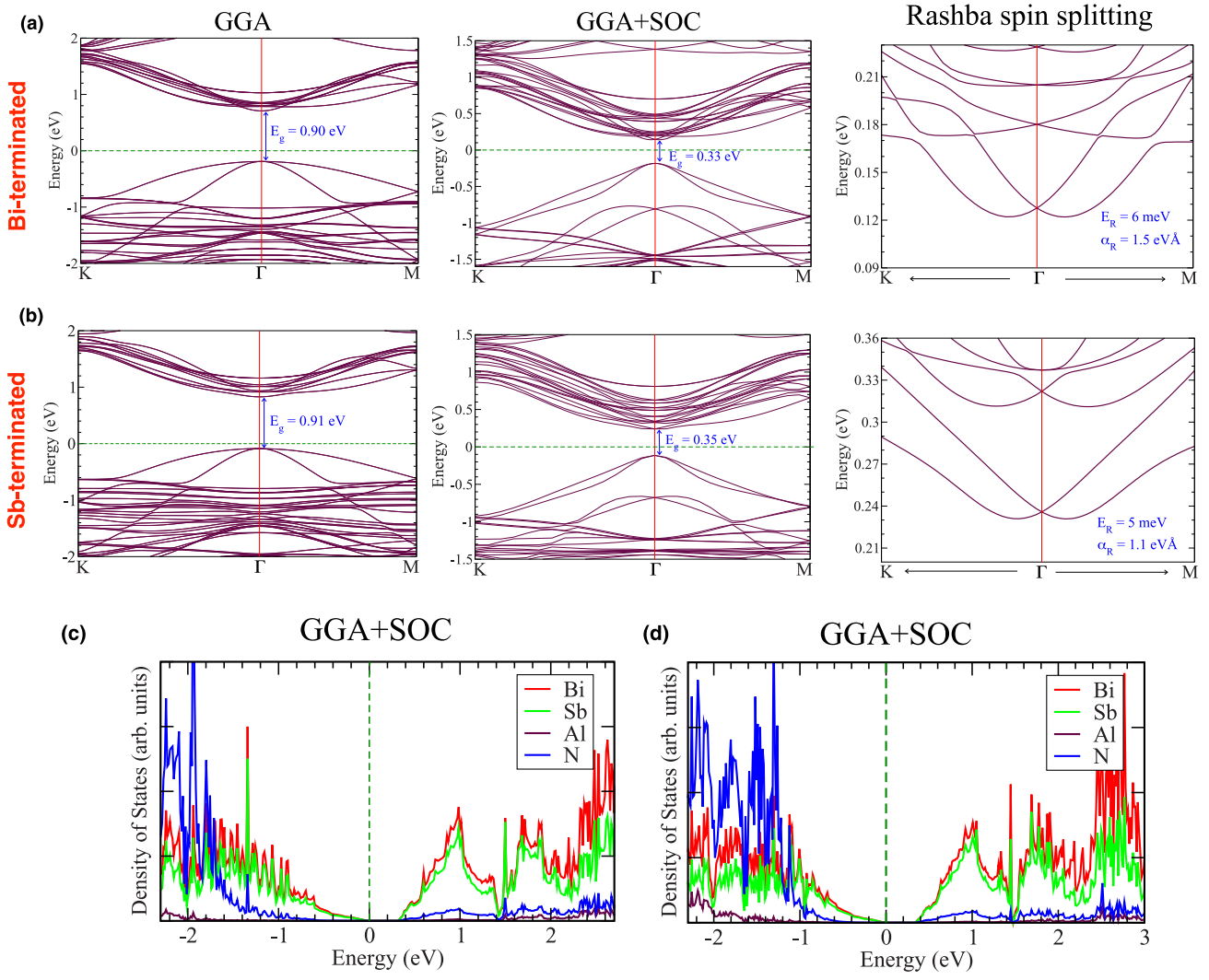


FIG. 7. Panel a (b) shows the electronic band structure calculated without SOC and with SOC and enlarged conduction bands showing Rashba spin splitting near the Fermi level for a Bi-terminated (Sb-terminated) interface. Panel c (d) depicts the projected DOS calculated using a Γ $k$-mesh of size 11 × 11 × 1 for a Bi-terminated (Sb-terminated) interface. The vdW interaction was included in all first-principles calculations for BiSb/AlN heterostructures. The green dotted line represents the Fermi level.

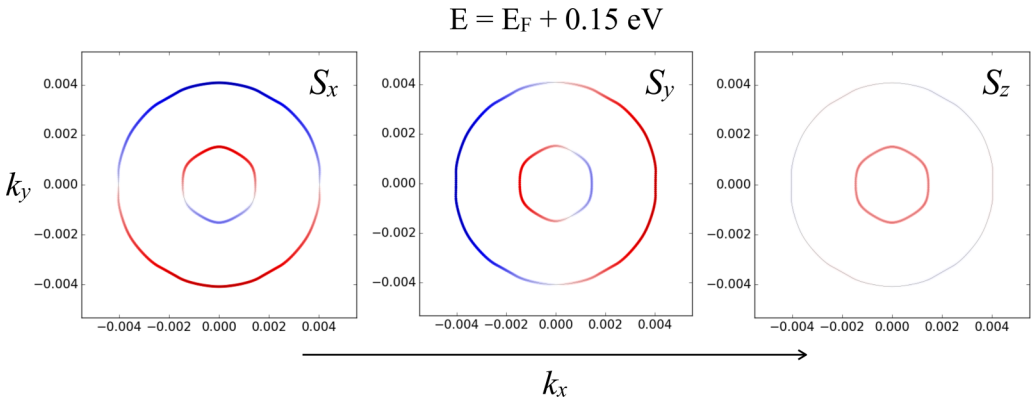


FIG. 8. Spin texture for a Bi-terminated interface calculated in a $k_x$-$k_y$ plane centered at the Γ point and at an energy surface 0.15 eV above the Fermi level. The color red depicts spin-up states while the color blue depicts spin-down states.

This particular feature has already been investigated for bulk BiSb [48]. We observe that the BiSb monolayer exhibits the same behavior upon reversal of the ferroelectric polarization.

The calculated electronic band structure and projected DOS of BiSb/AlN heterostructures are shown in Fig. 7. Figure 7(a) shows the electronic bands without SOC, with SOC, and conduction bands near the Γ point showing Rashba spin splitting for a Bi-terminated interface, while Fig. 7(b) shows the same but for an Sb-terminated interface. Without SOC, both Bi- and Sb-terminated heterostructures show a direct band gap of 0.90 and 0.91 eV at the Γ point, respectively. The CBB of both heterostructures has a free-electron gaslike parabolic shape near the Γ point, whereas the top valence bands are quite flat in both heterostructures indicating the presence of heavy holes along with existence of a light 2DEG at the interface. The direct gap of the heterostructures is lower compared to that of the isolated BiSb monolayer. Interestingly, we notice a Rashba-type spin splitting of the CBB in the presence of SOC for both heterostructures. Also, the direct DFT gap of both heterostructures reduces to 0.33 eV (Bi-terminated) and 0.35 eV (Sb-terminated) due to inclusion of SOC. The calculated strength of the Rashba spin splitting is $E_R = 6$ meV and $\alpha_R = 1.5$ eVÅ for the Bi-terminated interface and $E_R = 5$ meV and $\alpha_R = 1.1$ eVÅ for the Sb-terminated interface. The strength of the Rashba splitting is larger at the Bi-terminated interface. This is due to the fact that Bi has larger SOC compared to the Sb atom [62–65]. It is noteworthy that the strength of the Rashba spin splitting is amongst the largest yet known Rashba heterostructure systems. The reason for such a large Rashba splitting in this heterostructure system can be ascribed to the presence of Bi $6p$ and Sb $5p$ orbitals near the Fermi level as depicted by the projected DOS plots for both heterostructures [Figs. 7(c)–7(d)]. The semiconducting nature of both heterostructures is also evident from their respective DOS.

To further confirm the 2D nature of Rashba spin splitting, we calculate the spin projected spin texture in a $k_x$-$k_y$ plane centered at the Γ point. The constant energy (0.15 eV above the Fermi level) contour plots of the spin texture for the Bi-terminated interface are shown in Fig. 8. The spin texture for the Sb-terminated interface exhibits a similar shape. The circular shape of the spin textures confirms the purely 2D nature of the Rashba spin splitting of a 2DEG at the interface. Furthermore, we observe that only $S_x$ and $S_y$ spin components are present in the $k_x$-$k_y$ plane without the presence of any $S_z$ component. This indicates that the spin texture has only in-plane spin components. These remarkable giant Rashba features make this system suitable for many interesting applications in the spintronics industry. In particular, one can make highly efficient spin field-effect transistors using this system, where we exploit the giant 2D Rashba effect to control the spin state of the 2DEG.

In summary, we have identified a new energetically, dynamically, and mechanically stable crystal phase of the BiSb monolayer which has a buckled honeycomb lattice geometry. Our first-principles calculations reveal that this monolayer is a direct band gap semiconductor having free-electron-like parabolic conduction band features near the Γ point. Inclusion of SOC yields Rashba-type spin splitting of conduction bands near the Fermi level. The obtained Rashba spin splitting parameters ($E_R = 13$ meV, $\alpha_R = 2.3$ eVÅ) suggest that this system is amongst the largest yet known 2D Rashba semiconductors. The constant energy contour plots of spin texture confirm the purely 2D nature of Rashba splitting. Both BiSb/AlN heterostructures exhibit a direct band gap semiconducting nature having parabolic conduction bands near the Fermi level, which indicates the presence of a 2DEG at the interface. The strength of the Rashba splitting is stronger for the Bi-terminated interface ($E_R = 6$ meV, $\alpha_R = 1.5$ eVÅ) than for the Sb-terminated interface ($E_R = 5$ meV, $\alpha_R = 1.1$ eVÅ). The presence of a direct band gap with light electronlike features makes this system interesting for 2D optical device applications. Additionally, the existence of the 2D giant Rashba effect together with the electronic band gap in the visible range paves the way to use a BiSb monolayer and BiSb/AlN heterostructure systems in the development of highly efficient spin field-effect transistors and optoelectronics devices in the spintronics industry.

## ACKNOWLEDGMENTS

This work used the Extreme Science and Engineering Discovery Environment (XSEDE), which is supported by National Science Foundation Grant No. OCI-1053575. Additionally, the authors acknowledge support from Texas Advances Computer Center (TACC), the Bridges supercomputer at Pittsburgh Supercomputer Center, and the Super Computing

Systems (Spruce and Mountaineer) at West Virginia University (WVU). A.H.R. and S.S. acknowledge support from National Science Foundation (NSF) DMREF-NSF 1434897 project and DOE DE-SC0016176 project. S.S. thanks the donors of the Jefimenko family for their financial support through the Oleg D. and Valentina P. Jefimenko Physics Fellowship at WVU.

[1] K. v. Klitzing, G. Dorda, and M. Pepper, Phys. Rev. Lett. **45**, 494 (1980).
[2] D. J. Thouless, M. Kohmoto, M. P. Nightingale, and M. den Nijs, Phys. Rev. Lett. **49**, 405 (1982).
[3] E. I. Rashba, Fiz. Tverd. Tela **2**, 1224 (1960) [Sov. Phys. Solid State **2**, 1109 (1960)].
[4] K. Ishizaka *et al.*, Nat. Mater. **10**, 521 (2011).
[5] M. S. Bahramy, R. Arita, and N. Nagaosa, Phys. Rev. B **84**, 041202 (2011).
[6] D. Di Sante, P. Barone, R. Bertacco, and S. Picozzi, Adv. Mater. **25**, 509 (2013).
[7] E. Plekhanov, P. Barone, D. Di Sante, and S. Picozzi, Phys. Rev. B **90**, 161108 (2014).
[8] F.-X. Xiang, X.-L. Wang, M. Veldhorst, S.-X. Dou, and M. S. Fuhrer, Phys. Rev. B **92**, 035123 (2015).
[9] A. Narayan, Phys. Rev. B **92**, 220101 (2015).
[10] L. G. D. da Silveira, P. Barone, and S. Picozzi, Phys. Rev. B **93**, 245159 (2016).
[11] L. Leppert, S. E. Reyes-Lillo, and J. B. Neaton, J. Phys. Chem. Lett. **7**, 3683 (2016).
[12] T. Etienne, E. Mosconi, and F. De Angelis, J. Phys. Chem. Lett. **7**, 1638 (2016).
[13] Z.-G. Yu, J. Phys. Chem. Lett. **7**, 3078 (2016).
[14] J. Nitta, T. Akazaki, H. Takayanagi, and T. Enoki, Phys. Rev. Lett. **78**, 1335 (1997).
[15] A. D. Caviglia, M. Gabay, S. Gariglio, N. Reyren, C. Cancellieri, and J.-M. Triscone, Phys. Rev. Lett. **104**, 126803 (2010).
[16] Z. Zhong, A. Tóth, and K. Held, Phys. Rev. B **87**, 161102 (2013).
[17] S. LaShell, B. A. McDougall, and E. Jensen, Phys. Rev. Lett. **77**, 3419 (1996).
[18] Y. M. Koroteev, G. Bihlmayer, J. E. Gayone, E. V. Chulkov, S. Blügel, P. M. Echenique, and P. Hofmann, Phys. Rev. Lett. **93**, 046403 (2004).
[19] A. Varykhalov, D. Marchenko, M. R. Scholz, E. D. L. Rienks, T. K. Kim, G. Bihlmayer, J. Sánchez-Barriga, and O. Rader, Phys. Rev. Lett. **108**, 066804 (2012).
[20] C. R. Ast, J. Henk, A. Ernst, L. Moreschini, M. C. Falub, D. Pacilé, P. Bruno, K. Kern, and M. Grioni, Phys. Rev. Lett. **98**, 186807 (2007).
[21] J. D. Sau, R. M. Lutchyn, S. Tewari, and S. Das Sarma, Phys. Rev. Lett. **104**, 040502 (2010).
[22] J. D. Sau, S. Tewari, R. M. Lutchyn, T. D. Stanescu, and S. Das Sarma, Phys. Rev. B **82**, 214509 (2010).
[23] J. Alicea, Phys. Rev. B **81**, 125318 (2010).
[24] A. Das, Y. Ronen, Y. Most, Y. Oreg, M. Heiblum, and H. Shtrikman, Nat. Phys. **8**, 887 (2012).
[25] A. Kitaev, Ann. Phys. **303**, 2 (2003).
[26] J. C. Y. Teo and C. L. Kane, Phys. Rev. Lett. **104**, 046401 (2010).
[27] J. D. Sau, D. J. Clarke, and S. Tewari, Phys. Rev. B **84**, 094505 (2011).
[28] Z. Y. Zhu, Y. C. Cheng, and U. Schwingenschlögl, Phys. Rev. B **84**, 153402 (2011).
[29] Q. Liu, Y. Guo, and A. J. Freeman, Nano Lett. **13**, 5264 (2013).
[30] Y. Ma, Y. Dai, N. Yin, T. Jing, and B. Huang, J. Mater. Chem. C **2**, 8539 (2014).
[31] B. Amin, T. P. Kaloni, and U. Schwingenschlogl, RSC Adv. **4**, 34561 (2014).
[32] Q. Zhang and U. Schwingenschlögl, Phys. Rev. B **93**, 045312 (2016).
[33] S. Grytsyuk, A. Belabbes, P. M. Haney, H.-W. Lee, K.-J. Lee, M. D. Stiles, U. Schwingenschlögl, and A. Manchon, Phys. Rev. B **93**, 174421 (2016).
[34] Y. C. Cheng, Z. Y. Zhu, M. Tahir, and U. Schwingenschlögl, Europhys. Lett. **102**, 57001 (2013).
[35] A. C. Garcia-Castro, M. G. Vergniory, E. Bousquet, and A. H. Romero, Phys. Rev. B **93**, 045405 (2016).
[36] P. Hohenberg and W. Kohn, Phys. Rev. **136**, B864 (1964).
[37] W. Kohn and L. J. Sham, Phys. Rev. **140**, A1133 (1965).
[38] G. Kresse and J. Furthmüller, Phys. Rev. B **54**, 11169 (1996).
[39] G. Kresse and D. Joubert, Phys. Rev. B **59**, 1758 (1999).
[40] J. P. Perdew, K. Burke, and M. Ernzerhof, Phys. Rev. Lett. **77**, 3865 (1996).
[41] A. Togo, F. Oba, and I. Tanaka, Phys. Rev. B **78**, 134106 (2008).
[42] J. Heyd, G. E. Scuseria, and M. Ernzerhof, J. Chem. Phys. **118**, 8207 (2003).
[43] J. Heyd and G. E. Scuseria, J. Chem. Phys. **121**, 1187 (2004).
[44] A. Tkatchenko and M. Scheffler, Phys. Rev. Lett. **102**, 073005 (2009).
[45] T. Bučko, S. Lebègue, J. Hafner, and J. G. Ángyán, Phys. Rev. B **87**, 064110 (2013).
[46] A. H. Romero and F. Munoz, PYPROCAR code, 2015.
[47] S. Singh, W. Ibarra-Hernandez, I. Valencia-Jaime, G. Avendano-Franco, and A. H. Romero, Phys. Chem. Chem. Phys. **18**, 29771 (2016).
[48] S. Singh, A. C. Garcia-Castro, I. Valencia-Jaime, F. Muñoz, and A. H. Romero, Phys. Rev. B **94**, 161116 (2016).
[49] J. N. Coleman *et al.*, Science **331**, 568 (2011).
[50] C. Ataca, H. Şahin, and S. Ciraci, J. Phys. Chem. C **116**, 8983 (2012).
[51] W. Yu, C.-Y. Niu, Z. Zhu, X. Wang, and W.-B. Zhang, J. Mater. Chem. C **4**, 6581 (2016).
[52] J.-W. Jiang, B.-S. Wang, J.-S. Wang, and H. S. Park, J. Phys. Condens. Matter **27**, 083001 (2015).
[53] H. Zheng, X.-B. Li, N.-K. Chen, S.-Y. Xie, W. Q. Tian, Y. Chen, H. Xia, S. B. Zhang, and H.-B. Sun, Phys. Rev. B **92**, 115307 (2015).
[54] H. Wang, Q. Li, Y. Gao, F. Miao, X.-F. Zhou, and X. Wan, New J. Phys. **18**, 073016 (2016).
[55] P. G. Klemens, Phys. Rev. **148**, 845 (1966).
[56] D. König, K. Casalenuovo, Y. Takeda, G. Conibeer, J. Guillemoles, R. Patterson, L. Huang, and M. Green, Phys. E: (Amsterdam, Neth.) **42**, 2862 (2010).

[57] Q. Peng, C. Liang, W. Ji, and S. De, Comput. Mater. Sci. **68**, 320 (2013).
[58] Q. Peng, C. Liang, W. Ji, and S. De, Mech. Mater. **64**, 135 (2013).
[59] R. C. Andrew, R. E. Mapasha, A. M. Ukpong, and N. Chetty, Phys. Rev. B **85**, 125428 (2012).
[60] K. F. Mak, C. Lee, J. Hone, J. Shan, and T. F. Heinz, Phys. Rev. Lett. **105**, 136805 (2010).
[61] C. R. Ast and H. Höchst, Phys. Rev. Lett. **87**, 177602 (2001).
[62] L. E. Díaz-Sánchez, A. H. Romero, and X. Gonze, Phys. Rev. B **76**, 104302 (2007).
[63] L. E. Díaz-Sánchez, A. H. Romero, M. Cardona, R. K. Kremer, and X. Gonze, Phys. Rev. Lett. **99**, 165504 (2007).
[64] J. Serrano, R. K. Kremer, M. Cardona, G. Siegle, L. E. Díaz-Sánchez, and A. H. Romero, Phys. Rev. B **77**, 054303 (2008).
[65] W. Ibarra-Hernández, M. J. Verstraete, and J.-Y. Raty, Phys. Rev. B **90**, 245204 (2014).